# CHAPTER IV
# RESULTS AND DISCUSSION

## 4.1 Carbon Dioxide Solubility

When carbon dioxide bubbles in water, carbonic acid, bicarbonate, carbonate and hydrogen ions are formed in the solution (reaction 4.1). The measurement of the solution pH with time is the in-direct way to observe the solubility of carbon dioxide as shown in Figure 4.1. The pH of solution was gradually decreased from 8.26 to 6.02 and reached equilibrium within 80 min.

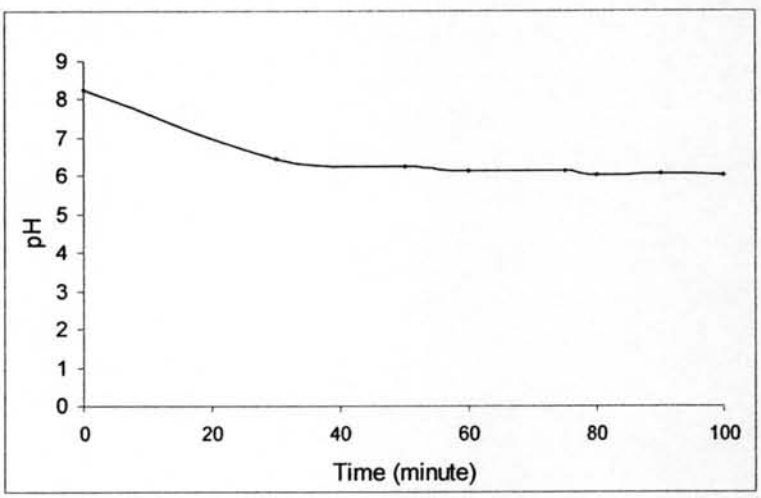


Figure 4.1 The variation of pH with time of simulated produced water at 30°C.

Since the dissociation constant of reaction (4.3) is much less than that of reaction (4.2), the second dissociation reaction is assumed to be neglected. Therefore, the bicarbonate ion, predominant species is formed from the first dissociation of carbonic acid only.

$$CO_2 + H_2O \longrightarrow H_2CO_3 \quad (4.1)$$

$$H_2CO_3 \longrightarrow H^+ + HCO_3^- \quad K_{a1} = 2.5 \times 10^{-4}\ \text{mol/L} \quad (4.2)$$

$$HCO_3^- \longrightarrow H^+ + CO_3^{2-} \quad K_{a2} = 5.60 \times 10^{-11}\ \text{mol/L} \quad (4.3)$$

## 4.2 The Influence of Temperature

Temperature is one of important parameters in the determination of the kinetics of chemical reaction including corrosion. In this experiment, the temperature was varied from 30°C to 60°C in temperature-controlled water bath. Simulated produced water saturated with carbon dioxide was used as a corrosive solution.

Figures 4.2 a) – d) show the surfaces of 13Cr and L80 coupons before exposing to the corrosive condition. They were used as received, no grinding and polishing in order to closely represent actual tubing used in production wells.

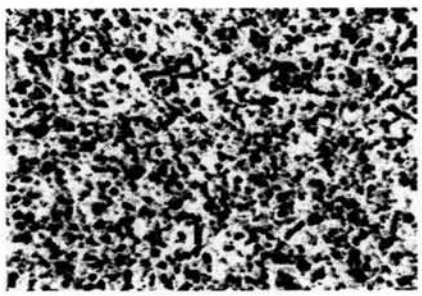

a) 13Cr at 40X

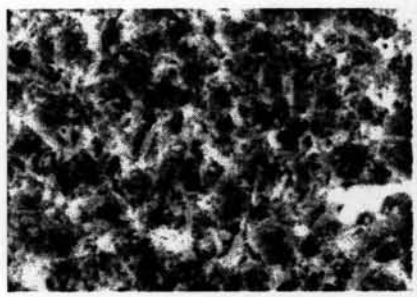

b) 13Cr at 200X

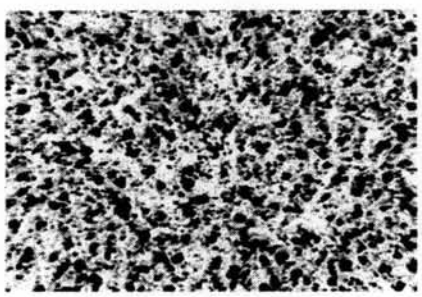

c) L80 at 40X

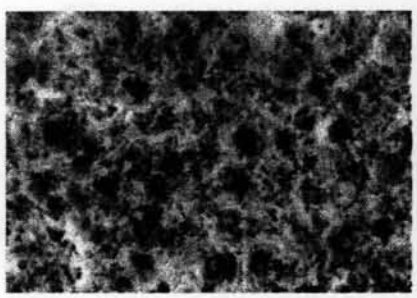

d) L80 at 200X

Figure 4.2 Opticalmicrophotograph of the surface before exposure in the corrosive solution of a) 13Cr at 40X, b) 13Cr at 200X, c) L80 at 40X, and L80 at 200X .

The roughness and the degree of roughness of two surfaces were the same. After exposure, there was black film of magnetite ($Fe_3O_4$) covering the surface of L80 both at 30 °C and 60 °C (Figures 4.3 a) and b)) and the roughness of the surface seemed to be smooth. However, the surface of 13Cr steels did not show any significant change. There were some deeper areas as shown in Figure 4.3 c) and d).

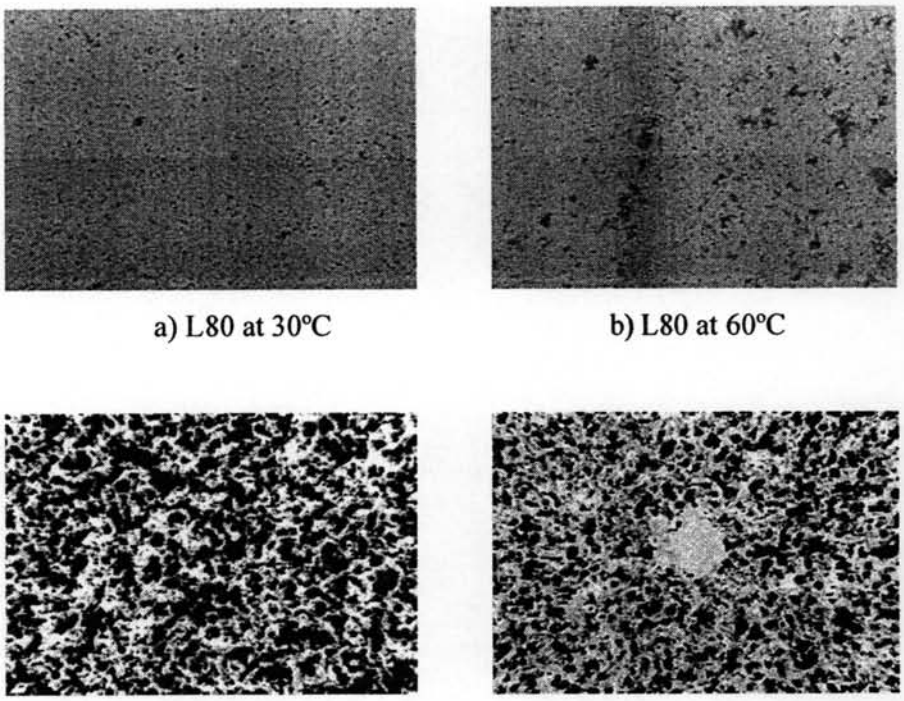

a) L80 at 30°C b) L80 at 60°C

c) 13Cr at 30°C d) 13Cr at 60°C

Figure 4.3 Optical microphotograph at 40X of surfaces after exposure of the coupons in simulated produced water at the $CO_2$ presence of 1 atmosphere of a) L80 30°C, b) L80 at 60°C, c) 13Cr at 30°C, and d) 13Cr at 60°C.

Polarization curves of L80 are shown in Figures 4.4 a) - c) where the corrosion potential remains unchanged with temperature. The constant corrosion potential resulted from the constant oxidizing power of solution. Therefore, the increase in corrosion rate due to the temperature was not resulted from the aggressiveness of the solution but kinetic aspects.

Polarization curves of 13Cr show that the corrosion potentials were not affected by temperature, however, there was passive layer formation as shown by the flat region in Figures 4.5 a) – c). It was found that pitting potential (the potential at which passive film is destroyed) decreased from 0.09 V to - 0.04 V as temperature increased from 30°C to 60°C. The decrease in the pitting potential resulted in a shorter passive region, which implied that the increase in temperature leaded to destabilization of passive film on the surface of stainless steel.

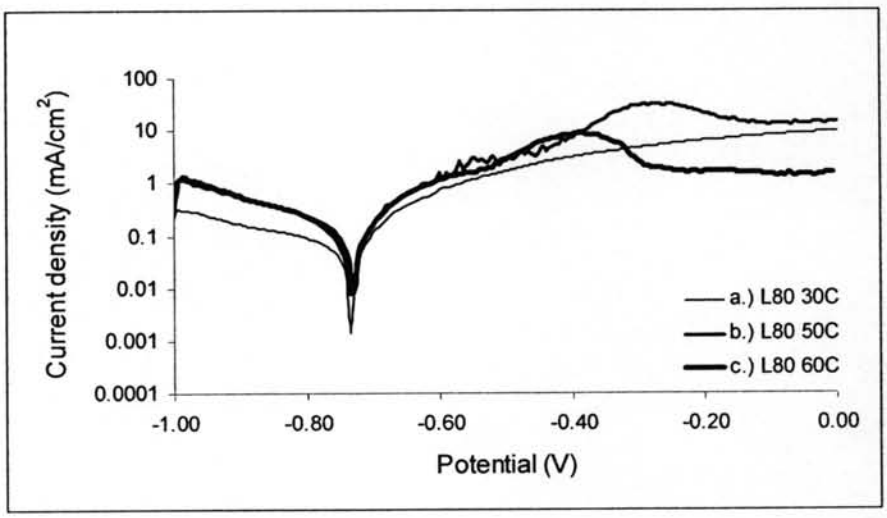


Figure 4.4 The polarization curve of L80 in simulated produced water saturated with $CO_2$ at 30°C - 60°C.

The examples of corrosion rate calculation for both immersion technique and potentiodynamic polarization are given in the Appendix B and C.

The comparison of corrosion rates of two materials from both techniques is given Figure 4.6. The corrosion rate of L80 from the polarization technique was much more affected by temperature than that from the immersion test. However, the corrosion rate of 13Cr from both techniques was similar, which was slightly increased with temperature.

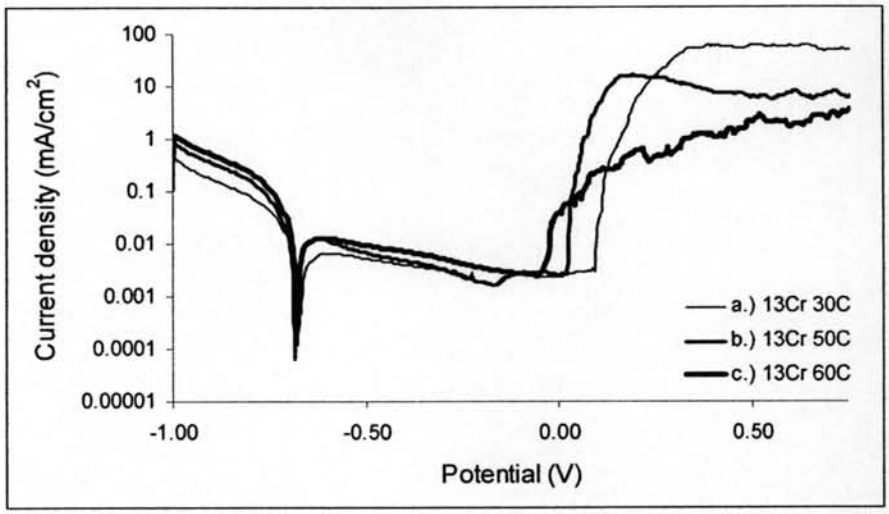


Figure 4.5 The polarization curve of 13Cr in simulated produced water saturated with $CO_2$ at 30°C - 60°C.

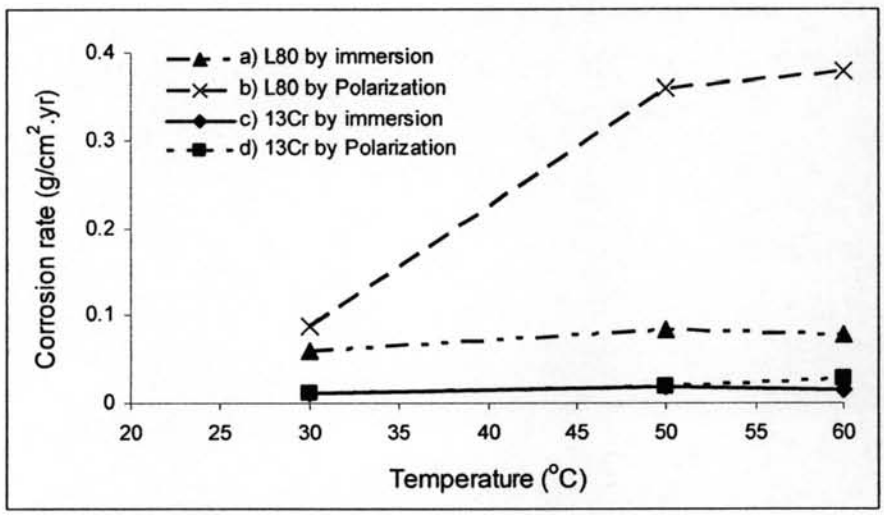


Figure 4.6 Corrosion rates of 13Cr and L80 in simulated produced water saturated with $CO_2$ at various temperatures obtained from immersion and potentiodynamic polarization techniques.

### 4.3 The influence of Chloride Concentration

Chloride ions were varied by adjusting the concentration of NaCl in the solution, i.e. 0.1%NaCl, 1%NaCl and 3.5%NaCl. Other components such as KCl, $CaCl_2$, $MgCl_2$ and $NaHCO_3$ were kept constant. The experiments were done at 60°C and the solution was saturated with $CO_2$.

The specimens were visually examined. There was no localized attack by chloride observed on both materials. However, microscopic inspection revealed that a highly spread non-uniform attack did occur especially on 13Cr, as shown in Figures 4.7 a) and b). The higher chloride contents cause the higher pitting tendency, as also reported by other investigations (Sun *et al*, 2003 and Ateya *et al*, 2002). The surfaces of L80 were not affected by chloride contents as shown in Figures 4.7 c) and d).

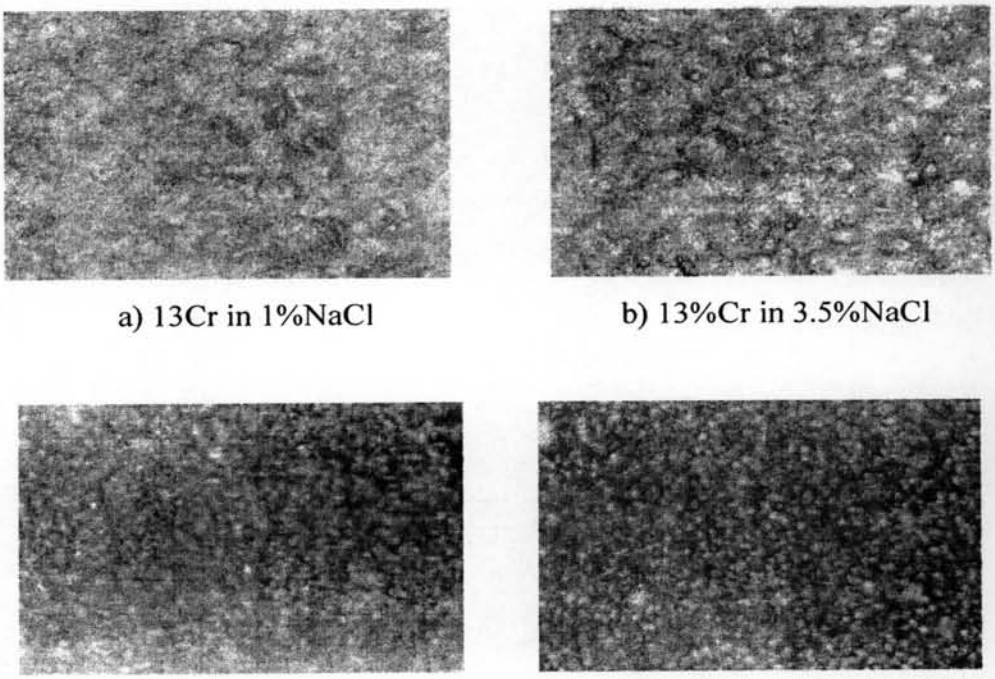

a) 13Cr in 1%NaCl

b) 13%Cr in 3.5%NaCl

c) L80 in 1%NaCl

d) L80 in 3.5%NaCl

Figure 4.7 Optical microphotograph at 100X of surfaces after exposed in NaCl solution of a) 13Cr in 1%NaCl, b) 13%Cr in 3.5%NaCl, c) L80 in 1%NaCl, and d) L80 in 3.5%NaCl.

The polarization curves of 13Cr as shown in Figure 4.8 illustrate that the passive current became noisy as chloride concentration increased, and sequentially, the passive film become unstable. Therefore, increasing of the chloride ions resulted in decreasing of pitting potential, shortening the passive region, and breaking the passive film. When the 13Cr was no longer passivated by passive film, the bared metal was locally attacked by the corrosive solution. Thus, it seemed reasonable to suggest that the chloride ions leaded to the localized corrosion whereas the uniform corrosion was not affected.

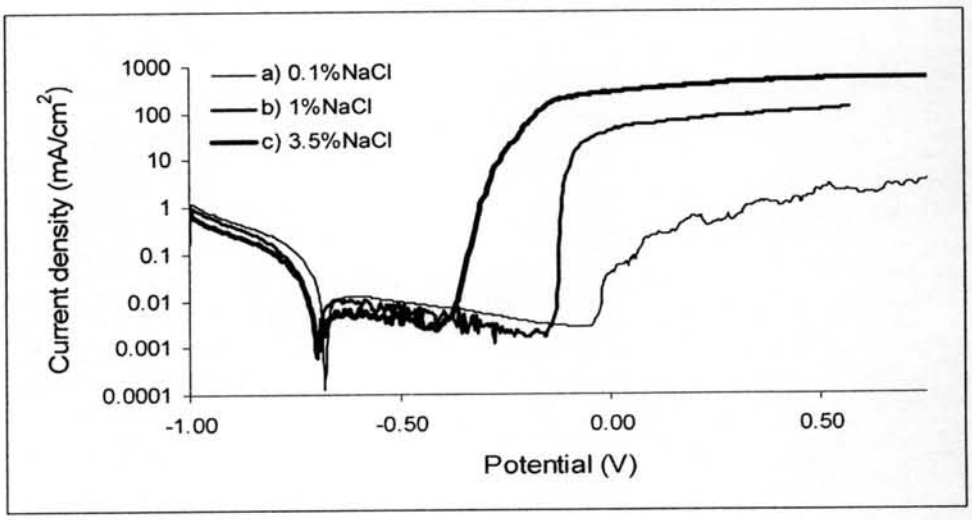


Figure 4.8 The polarization curve of 13Cr in simulated produced water saturated with $CO_2$ at 60°C in 0.1%NaCl - 3.5%NaCl.

It was found for L80 (Figure 4.9) that the corrosion potentials were virtually unchanged with chloride ions indicated that the oxidizing power of solution was not increased with chloride contents. The higher corrosion rate was obtained from the polarization test than that from the immersion test, however 13Cr showed contrast results and chloride ions showed insignificant effect in the potentiodynamic polarization measurement.

Corrosion rates of L80 and 13Cr are shown in Figure 4.10. Corrosion rates of L80 and 13Cr tended to increase with chloride concentration.

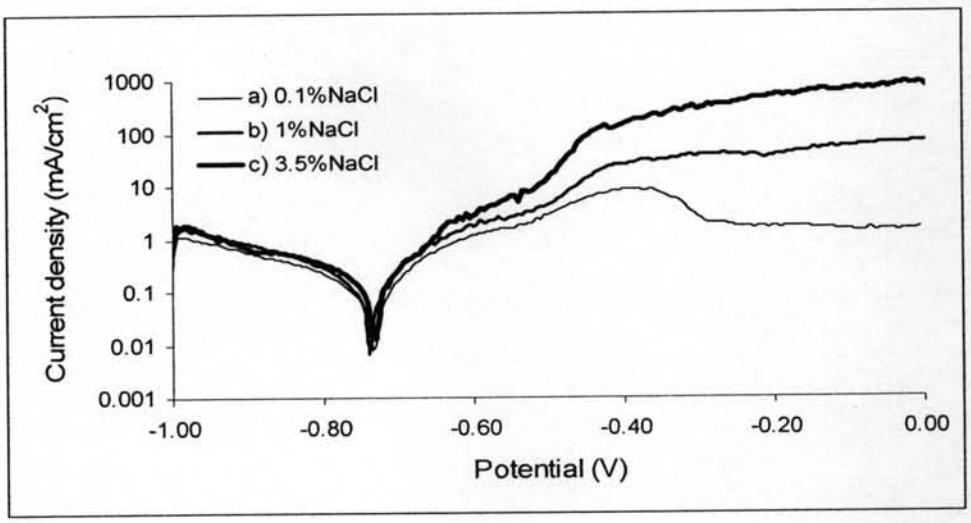


Figure 4.9 The polarization curves of L80 in simulated produced water saturated with $CO_2$ at 60°C in 0.1%NaCl - 3.5%NaCl.

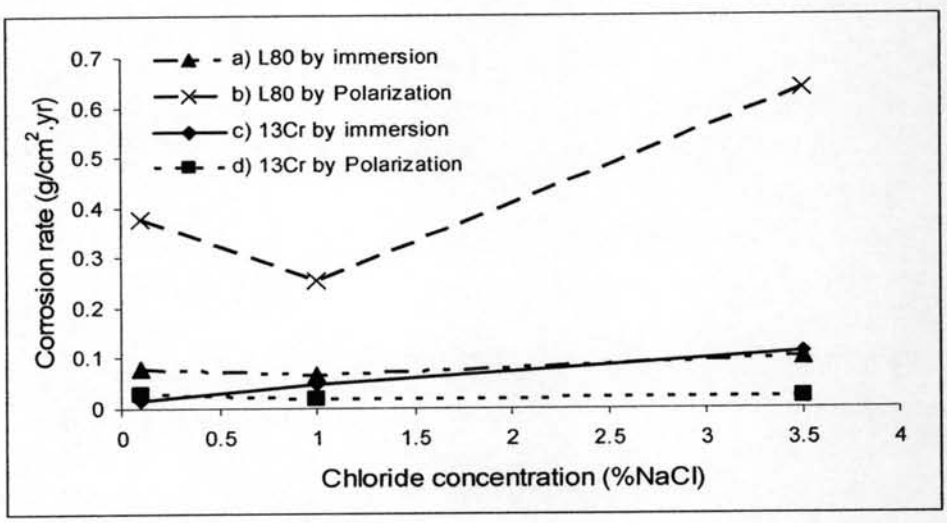


Figure 4.10 Corrosion rate of 13Cr and L80 in simulated produced water saturated with $CO_2$ at various chloride concentrations at 60°C.

## 4.4 The Influence of Carbon Dioxide Partial Pressure

Carbon dioxide is the key parameter in corrosion of natural gas production. These experiments were done in the simulated produced water at a constant temperature (60°C) and various partial pressures of $CO_2$, 0, 0.5, and 1 atmosphere.

Figures 4.11 a) and b) presents the surface of 13Cr after immersing in simulated produced water in the absence of $CO_2$ before and after cleaning with 10% $HNO_3$ solution, respectively. The appearance of 13Cr before and after cleaning was essentially not different which implies that the surface of 13Cr was less contaminated by corrosion product when the system is lack of $CO_2$. In addition, the appearances of the two coupons were similar to fresh coupons (Figure 4.2 a) and b)).

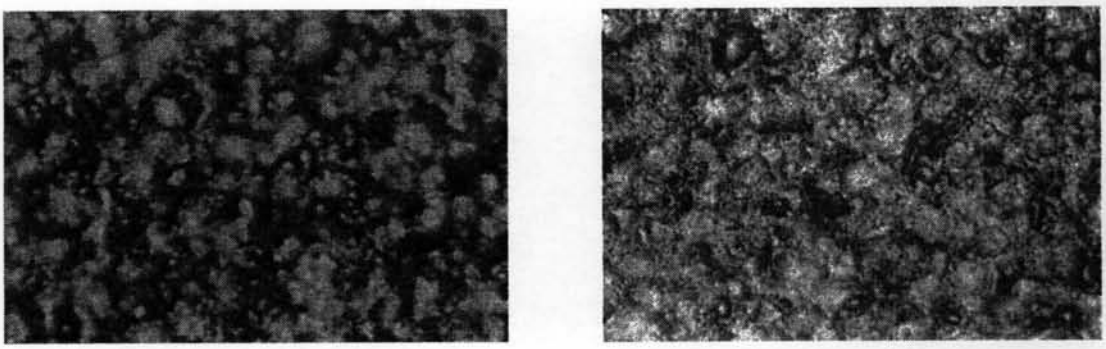

a) before cleaning with $HNO_3$ b) after cleaning with $HNO_3$

Figure 4.11 Optical microphotograph of 13Cr at 100X in simulated produced water in the absence of $CO_2$ and at 60°C a) before cleaning with $HNO_3$ and b) after cleaning with $HNO_3$.

On the contrary, surfaces of L80 shown in Figures 4.12 a) and b) were totally covered with black film of magnetite which can be removed by the cleaning solution of hexamethylene tetramine in 50%HCl.

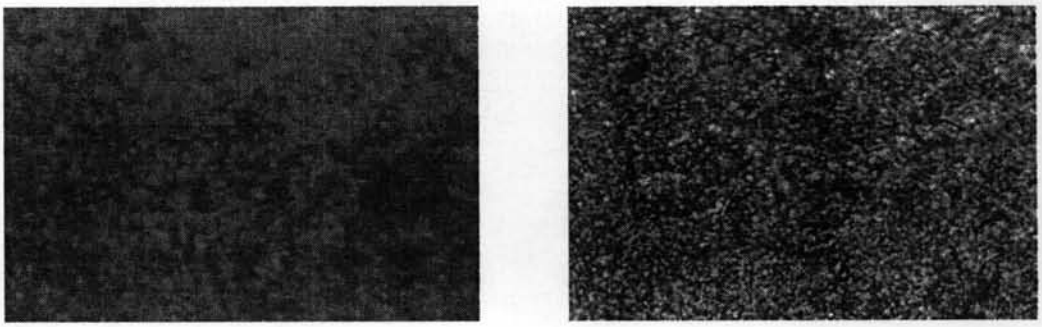

a) before cleaning b) after cleaning

Figure 4.12 Optical microphotograph of L80 at 100X in simulated produced water in the absence of $CO_2$ and at 60°C a) before and b) after cleaning with the solution of hexamethylene tetramine in 50% of HCl.

For L80, the polarization curve (Figure 4.13) shows greatly increase in the cathodic current. The corrosion potentials were -0.8730 V in the absence of $CO_2$ and increased to -0.751 V and -0.735 V as carbon dioxide partial pressure was 0.5 and 1.0 atmosphere, respectively. The significant increase in corrosion potential may come from the additional cathodic reaction, carbonic acid reduction and hydrogen evolution. This possibly proposed that carbon dioxide increase the oxidizing power of the solution. Similarly, the increasing in corrosion potential was also observed in the case of 13Cr. The corrosion potential (Figure 4.14) was increased from -0.8780 V to -0.7250 V and -0.6778 V as partial pressure of carbon dioxide is 0 to 0.5 and 1.0 atmosphere, respectively. Additionally, the pitting potential in the carbon dioxide-saturate solution was suddenly decreased, which confirmed the effect of carbon dioxide on increasing the possibility of pitting corrosion on stainless steel.

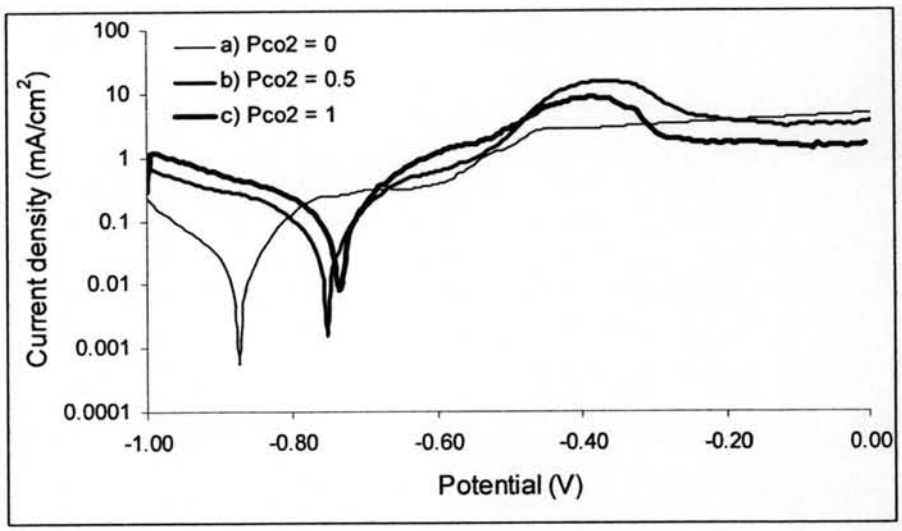


Figure 4.13 The polarization curve of L80 in simulated produced water at 60°C and $P_{CO2}$ = 0 - 1.0 atmosphere.

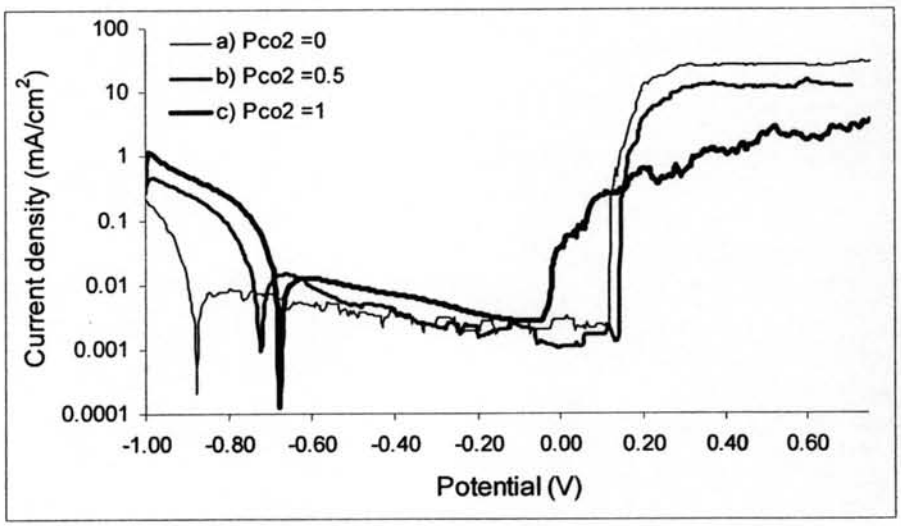


Figure 4.14 The polarization curve of stainless steel (13Cr) in simulated produced water at 60°C and $P_{CO2}$ = 0 - 1.0 atmosphere.

The relationship between corrosion rate and $P_{CO2}$ of 13Cr and L80 are given in the Figure 4.15. In all cases, the 13Cr was very resistible to the corrosion compared to that of L80. The 13Cr coupons were slightly affected by carbon dioxide

partial pressure. From the immersion test, the corrosion rate of 13Cr was 0.0037 g/cm$^2$.yr in the absence of $CO_2$ and increased to 0.0137 and 0.0150 g/cm$^2$.yr at the $P_{CO2}$ equal 0.5 and 1 atm, respectively. Therefore, $CO_2$ seemed to have slight effect on the 13Cr. In addition, these results were agreed with that from the potentiodynamic polarization technique. On the contrary, the results of L80 from the immersion test were not corresponded with potentiodynamic polarization technique and the corrosion rate of 13Cr was admittedly lower than that of L80. For L80, its oxide was able to react with the dissolved carbon dioxide to produce ferrous carbonate and a dissolved complex of iron, $Fe(CO_3)_2^{2-}$, which accelerated the dissolution of iron element (Linter *et al*, 1999). The higher the carbon dioxide presents, the higher the iron dissolves. In the case of 13Cr, it was not affected because its surface was passivated by rich oxide film of chromium oxide and chromium can not form a complex with the dissolved $CO_2$. Thus, the 13Cr was much less depended on $CO_2$ compare to that of L80.

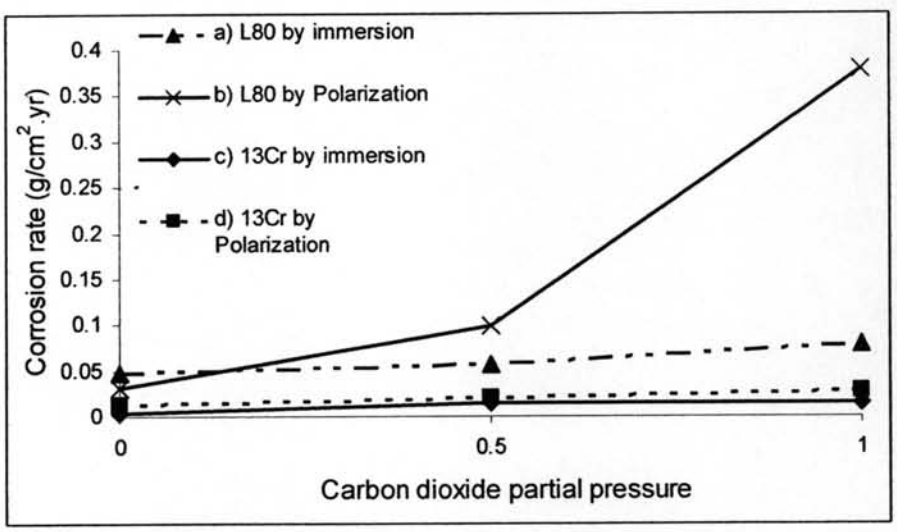


Figure 4.15 Corrosion rates of 13Cr and L80 in simulated produced water at 60°C with a variation of carbon dioxide partial pressure.

## 4.5 The Influence of pH of Solution

The pH of corrosive solution was varied from 5 to 12 and heated to 60°C and saturated with $CO_2$.

The surfaces of corroded coupons in simulated produced water solution saturated with $CO_2$ were examined at pH of 5.3. Figures 4.16 and 4.17 show the micrographs of the surface of 13Cr and L80 before and after cleaning.

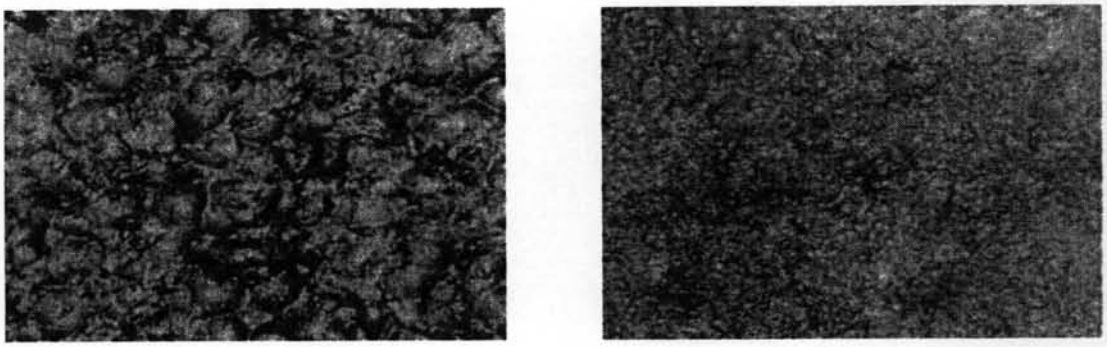

a) before cleaning with 10%$HNO_3$ b) after cleaning with 10%$HNO_3$

Figure 4.16 Optical microphotographs at 100X of the surface of 13Cr in simulated produced water at pH 5.12 a) before and b) after cleaning with 10%$HNO_3$.

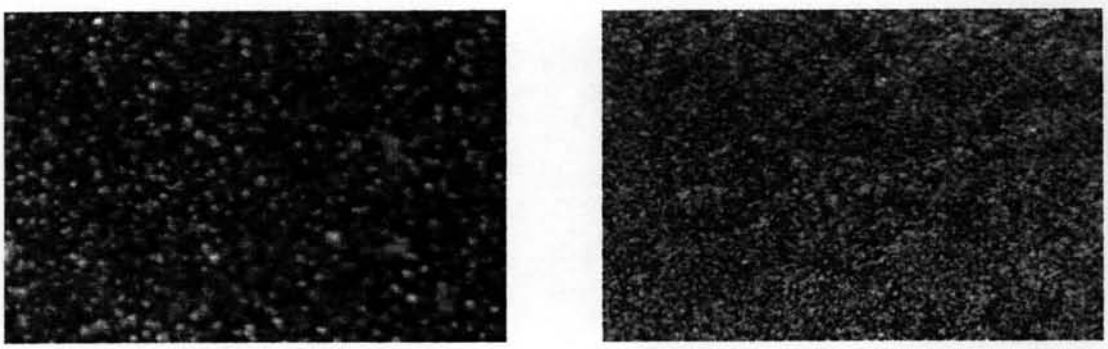

a) before cleaning b) after cleaning

Figure 4.17 Optical microphotographs at 100X of the surface of L80 in simulated produced water at pH 5.12 a) before and b) after cleaning with 3.5 grams of hexamethylene tetramine in 50% HCl solution.

The effect of pH on L80 is indicated by the polarization curves shown in the Figure 4.18. The highest corrosion potential of -0.7227 V was observed in the acidic environment and decreased to -0.7315 V and -0.7462 V at pH 8.12 and 11.34, respectively. Therefore, the aggressiveness of corrosive solution was increase by the acidity which enhanced the rate of hydrogen evolution due to the abundance of protons. At pH of 11.34, where the corrosion rate was the lowest, the current observed in the potential range of -0.4 V to -0.1 V was dropped. This region can be determined as pseudo-passivation of L80 due to the presence of hydroxyl, carbonate and bicarbonate ions. D.A.Lopez *et al.* (2003) suggested that, those ions can decrease the solubility of $FeCO_3$, which in turn made the formation of a protective film more feasible.

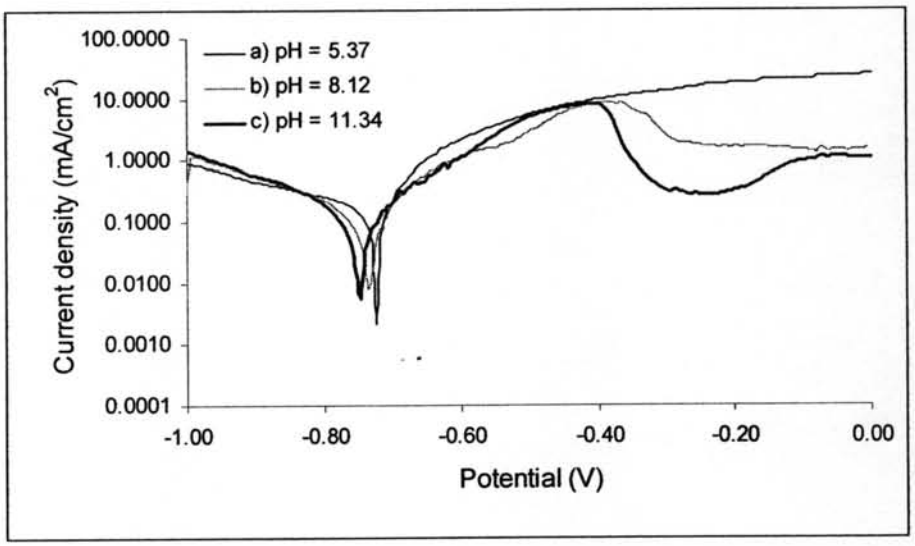


Figure 4.18 The polarization curve of L80 in various pH of simulated produced water saturated with $CO_2$ at 60°C.

The influence of pH on 13Cr (Figure 4.19) showed that the corrosion potential was higher and the passive region was shorter as the acidity was increased which meant that the passive film was destroyed faster in the acid solution.

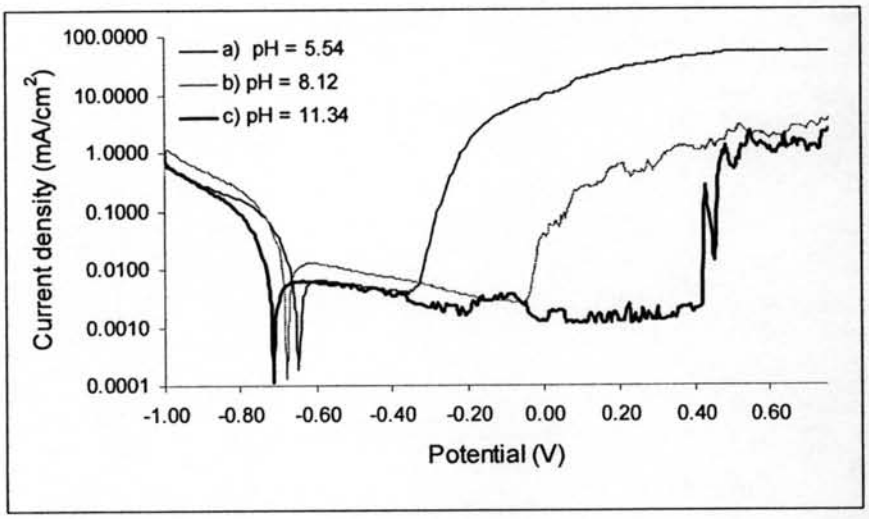


Figure 4.19 The polarization curve of 13Cr in various pH of simulated produced water saturated with $CO_2$ at 60°C.

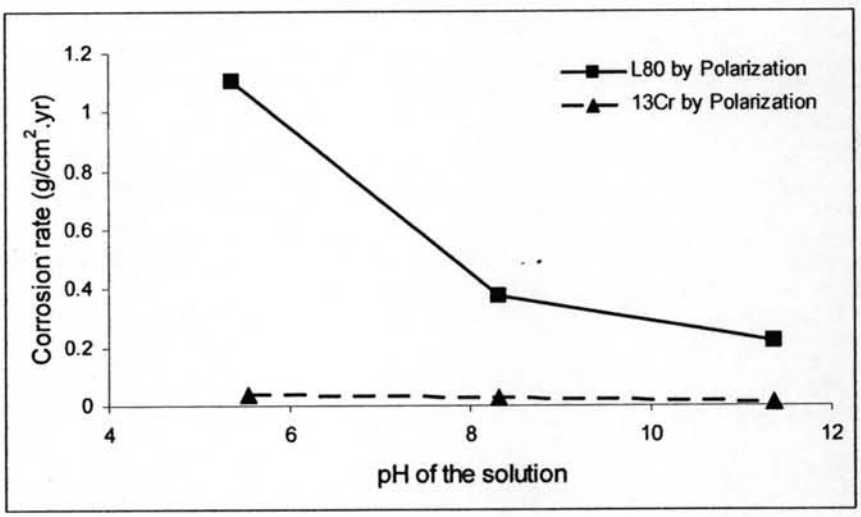


Figure 4.20 Corrosion rate of, a) 13Cr, and b) L80 in corrosive solution at various pH obtained from the potentiodynamic polarization technique.

The corrosion rates of 13Cr and L80 in corrosive solution at various pH obtained from polarization and immersion are shown in Figure 4.20 and 4.21, respectively. The results showed that the higher the pH, the lower the corrosion rate.

In addition the corrosion rate of 13Cr was decreased as pH was increased where the highest corrosion rate of 0.0588 g/cm$^2$.yr was observed in the acid solution (pH = 5.12). However, corrosion rate of L80 decreased when the corrosive solution became more basic.

In sum, investigations of pH suggested that the 13Cr is much more stable in a wide range of pH than L80.

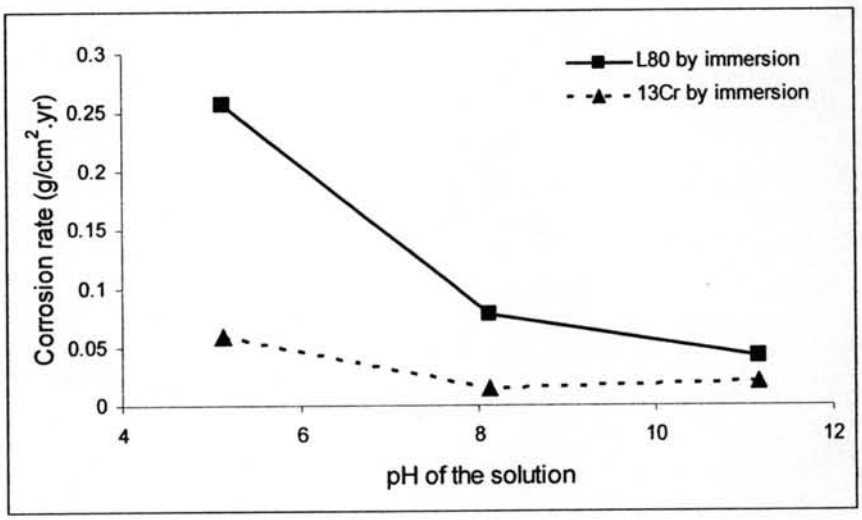


Figure 4.21 Corrosion rate in 60°C of corrosive solution at various pH obtained from the immersion test.

## 4.6 The Influence of Mercury

### 4.6.1 Mercury(II) and Temperature

In this section, the experiments were conducted at 30°C and 60°C and in the presence of one atmosphere of $CO_2$ solution. The concentrations of mercury(II) were varied from 0 to 12 ppm by polarization method where the polarization curves of 13Cr are shown in Figures 4.22 and 4.23, respectively. It was obviously noticed that pitting potential was increased when mercury(II) was added to the solution at both 30°C and 60°C. In 30°C, corrosion potential was essentially constant whereas the pitting potential was slightly increased. In addition, the slightly

decline in cathodic currents and corrosion rates were illustrated in the case of 60°C (Figure 4.23). Corrosion potential was decreased from -0.6778 V to -0.7110 V as 3 ppm mercury(II) was added. Further addition of mercury(II) to 6 and 12 ppm corrosion potential was slightly increased to -0.7050 V and -0.7016 V, respectively. The corrosion rates of 13Cr were not increased by the presence of mercury in the range of 0-12 ppm at both 30°C and 60°C (Figure 4.24).

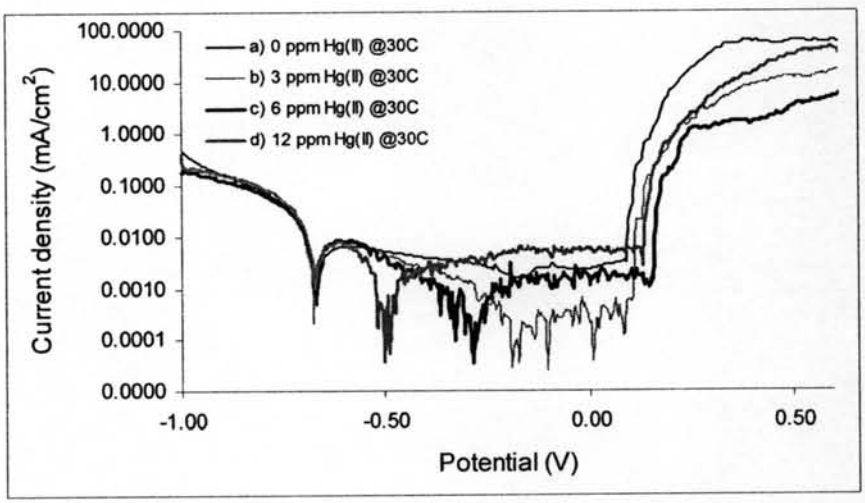


Figure 4.22 The polarization curve of 13Cr in 0-12 ppm of mercury(II) at 30°C.

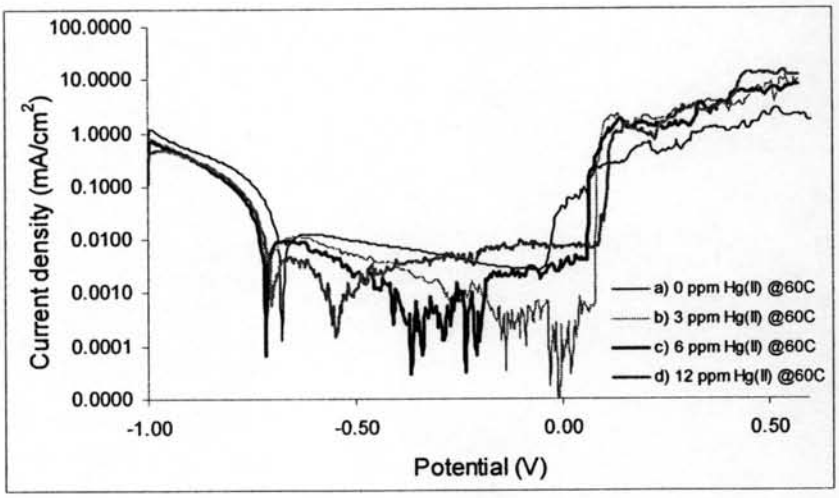


Figure 4.23 The polarization curve of 13Cr in 0-12 of mercury(II) at 60°C.

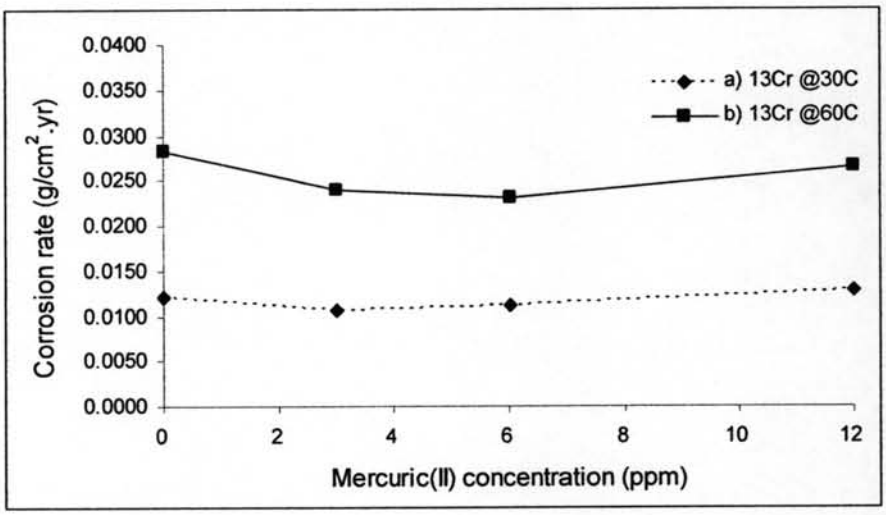


Figure 4.24 Corrosion rate comparison of 13Cr in 0-12 ppm Hg(II) solution saturated with carbon dioxide at 30°C and 60°C by using potentio dynamic polarization technique.

For L80, addition of small amount of mercury(II) (0-12 ppm) at 30°C and 60°C resulted in the slightly increase in corrosion potential as shown in Figures 4.24 – 4.25, however, it was not significantly changed with increasing temperature which implied that the oxidation of L80 was not affected by trace amount of

mercury(II). This was confirmed by Figure 4.26 a) and b) where the corrosion rates of L80 were not increased with the mercury(II).

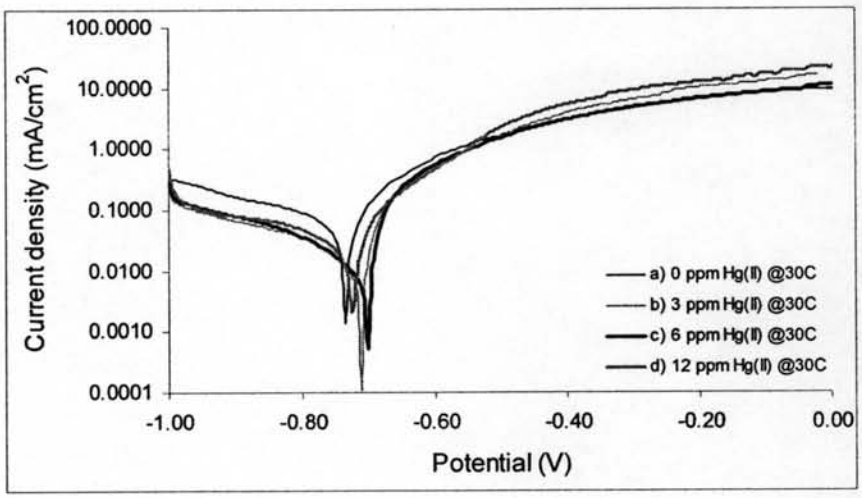


Figure 4.25 The polarization curve of L80 in various concentration of mercury(II) at 30°C.

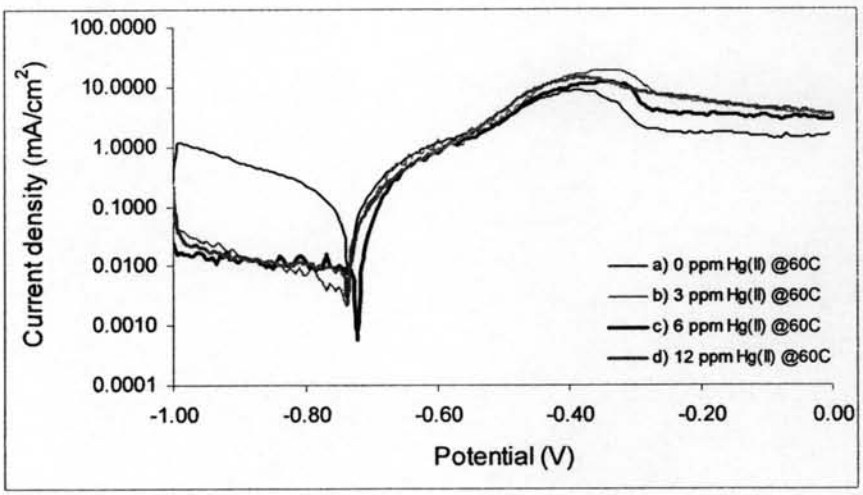


Figure 4.26 The polarization curve of L80 in various concentration of mercury(II) at 60°C.

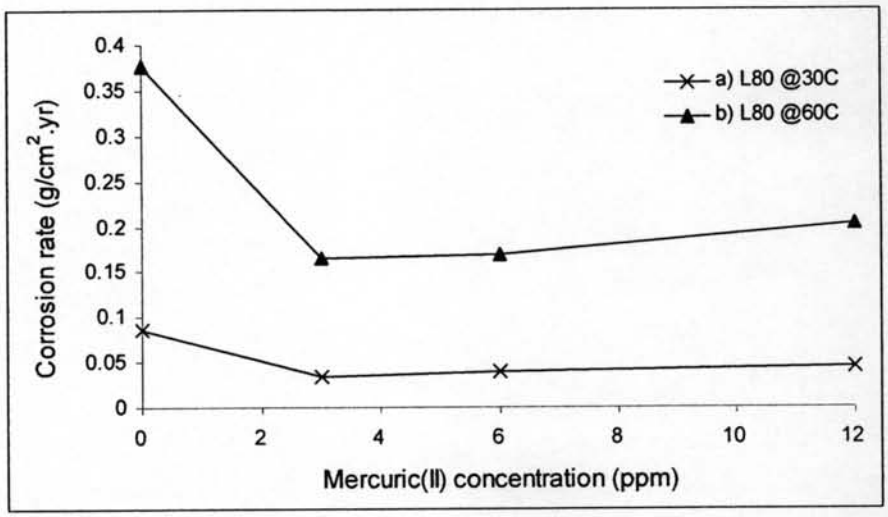


Figure 4.27 Corrosion rate comparison of L80 in 0-12 ppm Hg(II) solution saturated with carbon dioxide at 30°C and 60°C by using potentiodynamic polarization technique.

Immersion test of 13Cr and L80 at 6 and 12 ppm of mercury(II) and 60°C as compared to the polarization test are shown in Figure 4.28. Remarkably, the results of the immersion test showed that the 13Cr was much more influenced by mercury(II) than that in the polarization test. However, it seemed possible to propose that both materials were not suffered to the corrosion by mercury with the concentration less than 12 ppm.

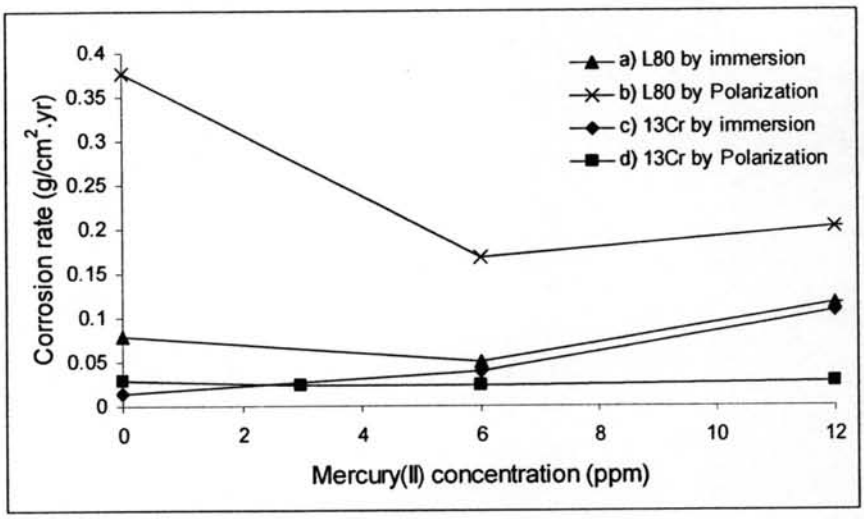


Figure 4.28 Corrosion rate of 13Cr and L80 in simulated produced water saturated with carbon dioxide at various mercury(II) concentrations at 60°C.

To attain more information about mercury(II), higher concentration (100 ppm and 1000 ppm) was studied. The potentiodynamic polarization curves of L80 (Figure 4.29) show that the corrosion potential was greatly increased from -0.7344 V to -0.4630 V when the mercury(II) was 1000 ppm.

To indicate the effect of mercury(II) to the L80 more clearly, the corrosion rates of L80 in 3 ppm to 1000 ppm mercury(II) are shown in Figure 4.30. It was easy to note that corrosion rate was slightly increased with mercury (0-100 ppm). With a mercury(II) concentration of 1000 ppm, the corrosion rate was found to be greatly increased. Therefore, it can be assumed that 100 ppm of mercury(II) was the corrosion limitation of L80 in saturated $CO_2$ solution at 60°C.

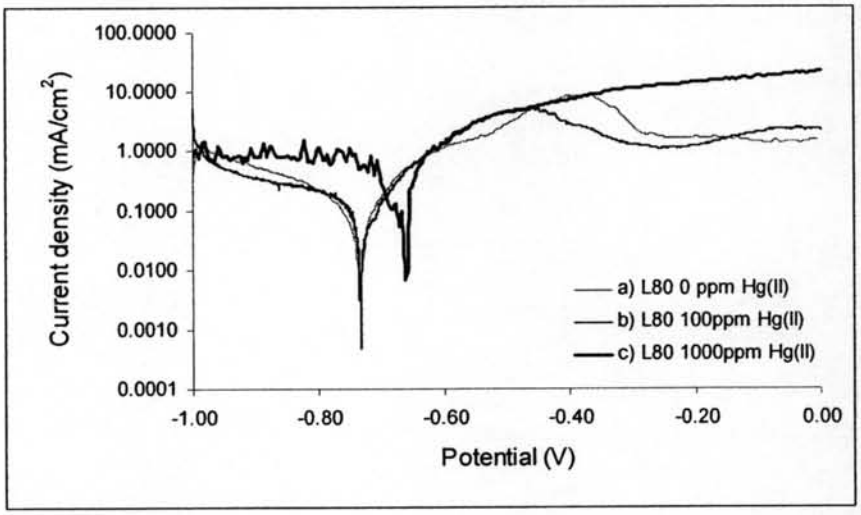


Figure 4.29 The polarization L80 in simulated produced water saturated with carbon dioxide at 60C in the presence of a) 0 ppm Hg(II) b) 100 ppm Hg(II) and c)1000 ppm Hg(II).

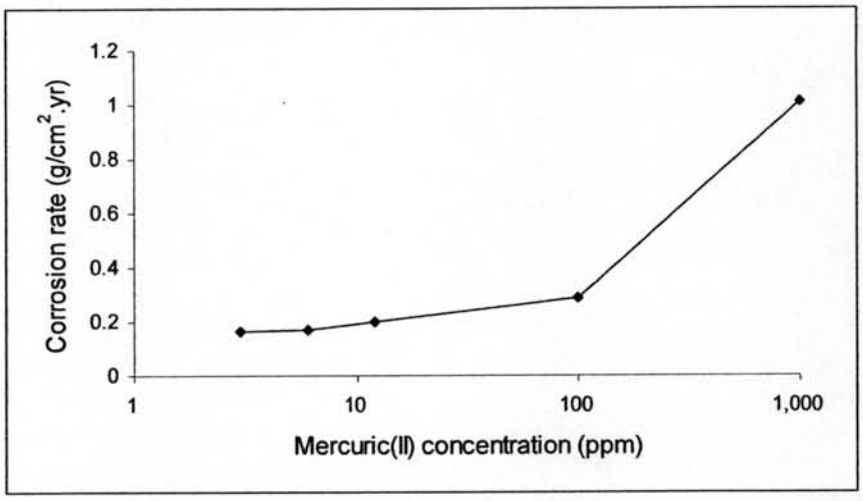


Figure 4.30 Corrosion rate of L80 in the various concentration of mercury(II), (0-1000 ppm), in simulated produced water saturated with carbon dioxide at 60°C.

On the other hand, the corrosion potential of 13Cr was greatly increased to -0.0253 V and -0.0186 V as 100 ppm and 1000 ppm of mercury(II) were added (Figure 4.31). Remarkably, corrosion current in 100 and 1000 ppm

mercury(II) was one and two order of magnitude higher than the absence of mercury(II) and the passive state of 13Cr was not observed.

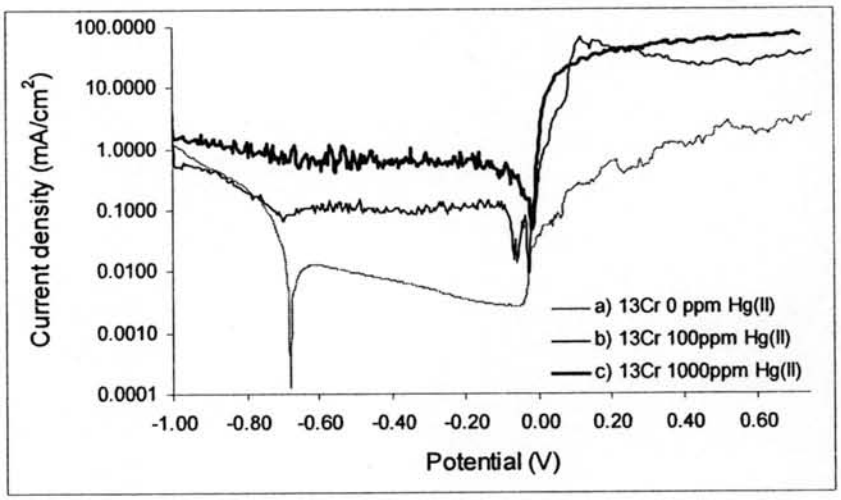


Figure 4.31 The polarization curve of 13Cr in simulated produced water saturated with carbon dioxide at 60C in the presence of a) 0 ppm Hg(II) b) 100 ppm Hg(II) and c)1000 ppm Hg(II).

From all of the findings, the corrosion rates of both materials were initially decreased and then gradually increased with an increasing of mercury(II). Therefore, it seemed reasonable to distinguish the passive film formed on the 13Cr surface by using chronoamperometry measurement.

### 4.6.2 Chronoamperometry of 13Cr

Chronoamperometry test for the passive film formation was studied at three concentrations of mercury(II) (Figure 4.32) and at potential of -0.4 V for 1 hour. Subsequently, the surface morphology after the chronoamperometry test was examined by Scanning Electron Microscope (SEM) (Figure 4.33 a) – c)) and Energy Dispersive X-Ray Fluorescence (Figure 4.34 a) and b)).

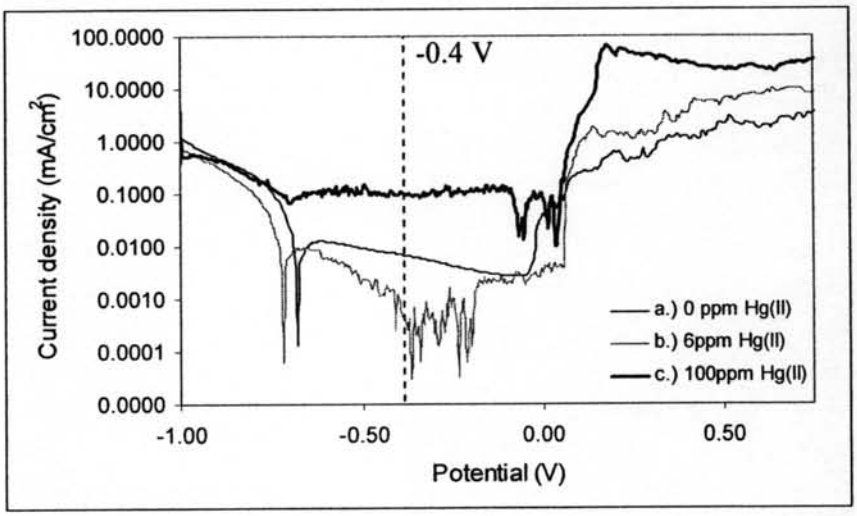


Figure 4.32 Polarization curve of 13Cr in 60°C solution with, a) 0 ppm of mercury(II), b) 6 ppm of mercury(II), and c) 100 of mercury(II) .

In the absence of mercury(II), XRD shows the corrosion product mainly in $Fe_3O_4$ and $Fe_2O_3$ instead of $FeCO_3$. Similar results were reported by Heuer *et al* (1999) where XPS was applied to examine the decomposition product of $FeCO_3$, chemically unstable component.

Furthermore, they proposed the decomposition mechanism of reagent grade $FeCO_3$ as shown in reactions (4.4) – (4.7).

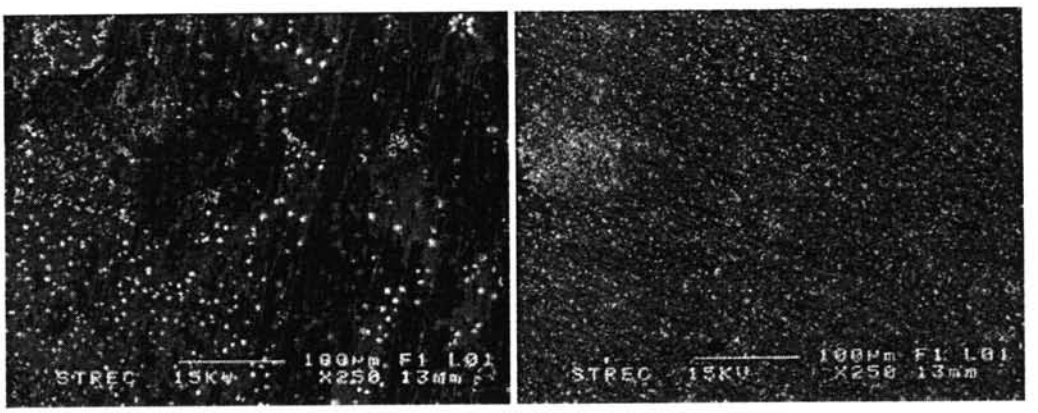


a) 0 ppm of mercury(II)

b) 6 ppm of mercury(II)

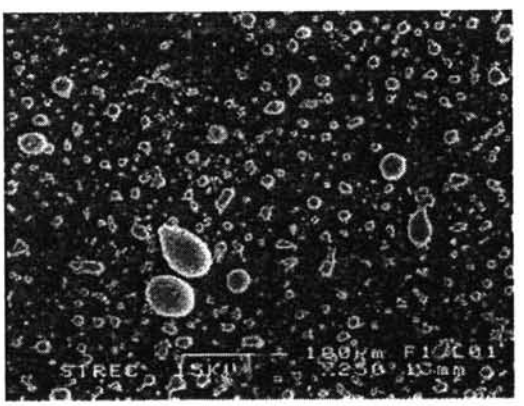

c) 100 ppm of mercury(II)

Figure 4.33 Scanning electron microphotograph of 13Cr in a) 0 ppm of mercury(II), b) 6 ppm of mercury(II), and c) 100 ppm of mercury(II) after chronoamperometry measurement at -0.4 V for 1 hour.

$$FeCO_3 \longrightarrow FeO + CO_2 \quad (4.4)$$

$$4FeO + O_2 \longrightarrow 2Fe_2O_3 \quad (4.5)$$

$$3FeO + CO_2 \longrightarrow Fe_3O_4 + CO \quad (4.6)$$

$$3FeO + H_2O \longrightarrow Fe_3O_4 + H_2 \quad (4.7)$$

They suggested that after the first decomposition, reaction (4.4), the resulting FeO may undergo additional transformations depend on the environmental condition. In the presence of oxygen FeO transforms quickly into $Fe_2O_3$, reaction (4.5), whereas reactions (4.6) and (4.7) indicate the reactions in the absence of oxygen. Upon the exposure to the oxygen, $Fe_3O_4$ transforms to the $Fe_2O_3$, reaction (4.8).

$$4Fe_3O_4 + O_2 \longrightarrow 6Fe_2O_3 \qquad (4.8)$$

Therefore, it might be presumed that the absence of $FeCO_3$ on the surface of 13Cr was due to reactions (4.4), (4.6), (4.7), and (4.8).

Surface of 13Cr in 6 ppm of mercury(II) (Figure 4.33 b) shows that $Fe_3O_4$ were dominant species presented and the existence of mercury(II) compound was not detected.

The surface morphology of 13Cr after exposed to the 100 ppm of mercury(II) as shown in Figure 4.33 c). Metal presented in the black area was the plain surface of pure Fe-Cr as confirmed by EDX measurement (Figure 4.34 a). The particles presented on the surface were not the mercury compounds but composed of NaCl, KCl, Fe, and Cr, which were precipitated from the major salts in the solution after finishing the chronoamperometry measurement (Figure 4.34 b).

In sum, at high concentration of mercury(II), the corrosion was considered to be very severe because of the abundance of mercury(II), which could be determined as the strong oxidizing agent or electrons consumer, due to the higher in electrode potential compare to hydrogen ions. Therefore, it can be said that the oxidizing power of solution or aggressiveness was extremely increased. However, the experiments show that the mercury(II) with the concentration less 12 ppm caused the slightly effect to the tubing steel made from L80 and 13Cr.

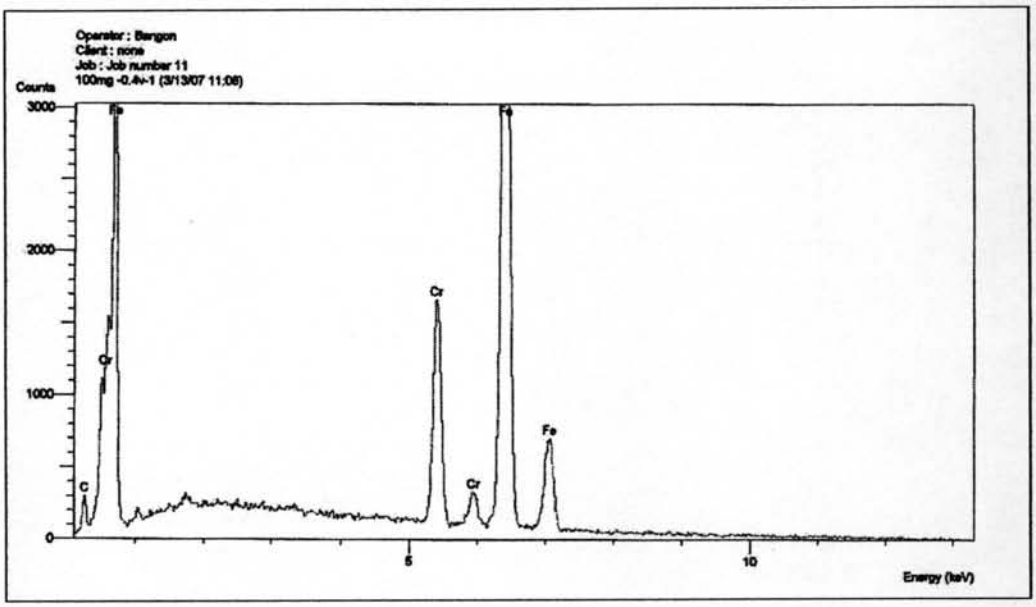


a)

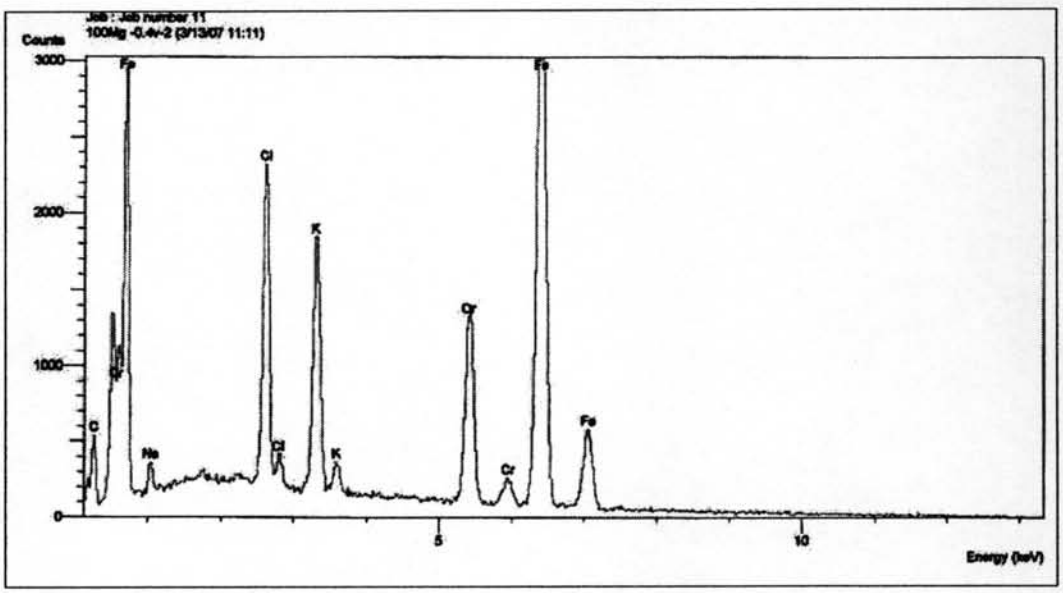


b)

Figure 4.34 EDX diagrams of 13Cr in 100 ppm of mercury(II) at 60°C observed at, a) plain surface and b) the particles presenting on the surface.

4.6.3 Mercury(II) and $P_{CO2}$

Carbon dioxide partial pressure was varied by co-introducing the nitrogen stream to the solution as same as in section 4.4. The addition in this section was that there was 3 ppm of mercury(II) existed in the simulated produced water.

Information from potentiodynamic polarization technique, i.e. corrosion potential, corrosion current density, pitting potential, and corrosion rate, are graphically presented in Figure 4.35 and 4.36 for L80 and 13Cr, respectively.

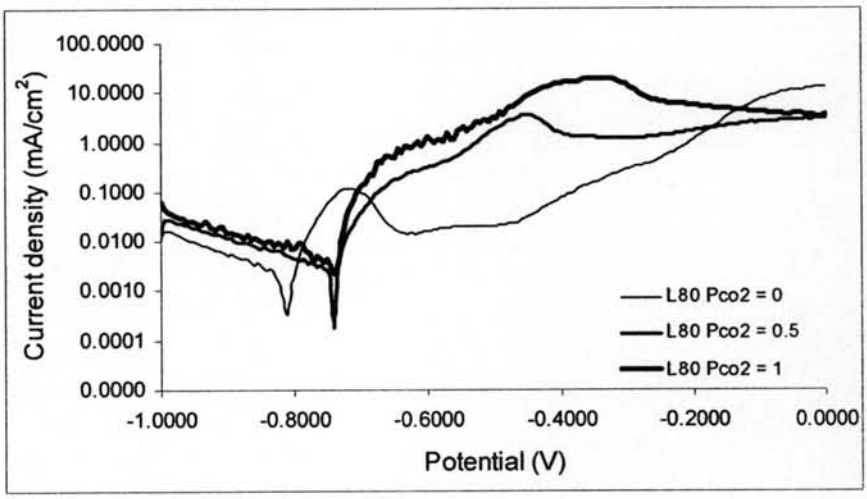


Figure 4.35 Polarization curve of L80 in 3 ppm mercury(II) under $P_{CO2}$ equal 0,0.5 and 1 at 60°C.

The corrosion rate of 13Cr shown in Figures 4.37 indicates that the corrosion rate was slightly increased with $P_{CO2}$ increased from 0.5 to 1.0 atmosphere. Similarly, the corrosion rates of L80 were also increased with the partial pressure of carbon dioxide as shown in Figure 4.38.

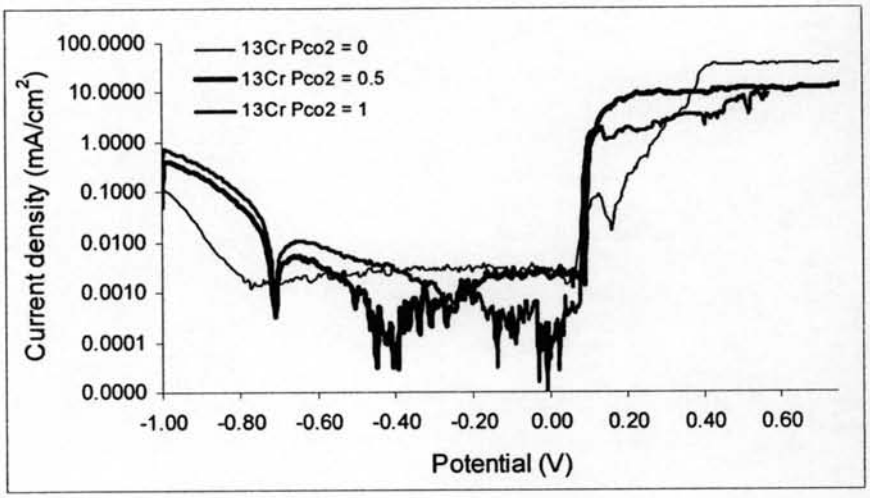


Figure 4.36 Polarization curve of 13Cr in 3 ppm mercury(II) under $P_{CO2}$ equal 0,0.5 and 1 at 60°C.

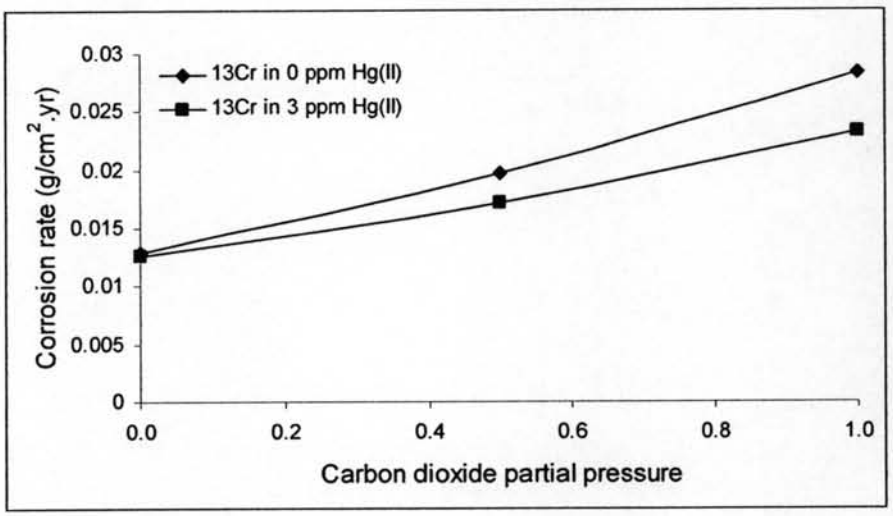


Figure 4.37 Corrosion rate comparison of 13Cr in 0 ppm and 3 ppm of mercury(II) saturated with $P_{CO2}$ = 0, 0.5 and 1.0 atmosphere.

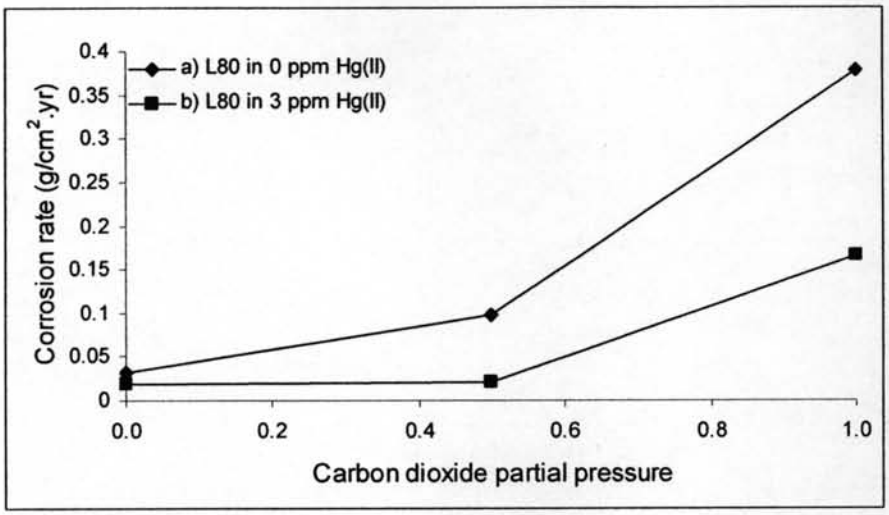


Figure 4.38 Corrosion rate comparison of L80 in 0 ppm and 3 ppm of mercury(II) saturated with $P_{CO2}$ = 0, 0.5 and 1.

Therefore, the result from this section was found to support the assumption that the addition of 3 ppm of merucy(II) leaded to the decrease in the corrosion rate of both materials as mentioned in the section 4.6.1.